ARL-TR-9420 ● MAY 2022

DEVCOM ARMY RESEARCH LABORATORY

Influence of Teeming Flux on Industrial-Scale Fe-Mn-Al-C Ingot Production

by Krista R Limmer, Edward J Horwath, and Daniel M Field

NOTICES

Disclaimers

The findings in this report are not to be construed as an official Department of the Army position unless so designated by other authorized documents.

Citation of manufacturer's or trade names does not constitute an official endorsement or approval of the use thereof.

Destroy this report when it is no longer needed. Do not return it to the originator.

ARL-TR-9420 ● MAY 2022

Influence of Teeming Flux on Industrial-Scale Fe-Mn-Al-C Ingot Production

Krista R Limmer, Edward J Horwath, and Daniel M Field
DEVCOM Army Research Laboratory

REPORT DOCUMENTATION PAGE

Form Approved
OMB No. 0704-0188

1. REPORT DATE *(DD-MM-YYYY)*	2. REPORT TYPE	3. DATES COVERED (From - To)
May 2022	Technical Report	July 2017–September 2019

4. TITLE AND SUBTITLE
Influence of Teeming Flux on Industrial-Scale Fe-Mn-Al-C Ingot Production

5a. CONTRACT NUMBER

5b. GRANT NUMBER

5c. PROGRAM ELEMENT NUMBER

6. AUTHOR(S)
Krista R Limmer, Edward J Horwath, and Daniel M Field

5d. PROJECT NUMBER

5e. TASK NUMBER

5f. WORK UNIT NUMBER

7. PERFORMING ORGANIZATION NAME(S) AND ADDRESS(ES)
DEVCOM Army Research Laboratory
ATTN: FCDD-RLW-MF
Aberdeen Proving Ground, MD 21005

8. PERFORMING ORGANIZATION REPORT NUMBER
ARL-TR-9420

9. SPONSORING/MONITORING AGENCY NAME(S) AND ADDRESS(ES)

10. SPONSOR/MONITOR'S ACRONYM(S)

11. SPONSOR/MONITOR'S REPORT NUMBER(S)

12. DISTRIBUTION/AVAILABILITY STATEMENT
Approved for public release: distribution unlimited.

13. SUPPLEMENTARY NOTES
ORCID IDs: Krista R Limmer, 0000-0003-4775-5876; Daniel M Field, 0000-0002-8890-4391

14. ABSTRACT
This report documents the characterization of Fe-Mn-Al-C steel ingot and slab sections produced during an industrial-scale trial heat. Optical microscopy and composition analysis were performed on sections of an as-normalized ingot and two partially broken-down slabs. Samples were examined from various locations along the length and depth of the ingots and slabs. The as-cast and partially recrystallized microstructures were evaluated and compared with Scheil simulation results. Composition analysis showed that the teeming flux selection affected the resulting ingot composition, whereas composition fluctuation in the ladle during teeming was not significant.

15. SUBJECT TERMS
FeMnAl, steel, ingot casting, low-density steel, metallography, Sciences of Extreme Materials

16. SECURITY CLASSIFICATION OF:			17. LIMITATION OF ABSTRACT	18. NUMBER OF PAGES	19a. NAME OF RESPONSIBLE PERSON
a. REPORT	b. ABSTRACT	c. THIS PAGE			Krista R Limmer
Unclassified	Unclassified	Unclassified	UU	36	19b. TELEPHONE NUMBER (Include area code) (410) 306-2039

Standard Form 298 (Rev. 8/98)
Prescribed by ANSI Std. Z39.18

Contents

List of Figures

List of Tables

Acknowledgments

The authors would like to gratefully acknowledge the team who supported the material production and characterization efforts. First, thank you to the industrial producers: Jim Kane and Darrin Schwartz from Ellwood Quality Steels, and Fred Fletcher and John Kross from ArcelorMittal Coatesville. Second, Katherine Sebeck from the US Army Combat Capabilities Development Command Ground Vehicle Systems Center for her involvement in the teeming flux selection, and William Herman from General Dynamics Land Systems for providing the local sample chemistry measurements. Third, Micah Gallagher and Jim Catalano at the US Army Combat Capabilities Development Command Army Research Laboratory for their assistance in sample preparation. Finally, we would like to express our appreciation to Colonel Ryan Howell and Bryan Cheeseman for their support of the Fe-Mn-Al-C production.

1. Introduction

Iron-manganese-aluminum-carbon (Fe-Mn-Al-C) alloy steels have been identified as potential lightweight alternatives for rolled homogeneous armor (RHA) that would provide nearly identical ballistic performance at equivalent thicknesses. The production of these new armor materials would use existing infrastructure and manufacturing facilities to produce rolled plate such that a dimensionally constant material thickness, with lower structure weight, could potentially be used anywhere RHA is employed.[1] Due to the high alloy content of Fe-Mn-Al-C alloys, domestic commercial scale-up of the manufacturing processes and ballistic test of wrought materials for plate Fe-Mn-Al-C alloys is being evaluated by the Army. Recent laboratory and industrial production trials and subsequent testing have demonstrated the feasibility of Fe-Mn-Al-C alloys to meet the desired mechanical and ballistic specifications.[2,3]

As identified in the previously reported first industrial-scale production of Fe-Mn-Al-C, the flux used during the casting process has a significant effect on the resulting quality and composition of the ingots.[4] This has also been reported as a significant concern in the slag development for continuous casting of Fe-Mn-Al-C alloys, with silica (SiO_2) content of the slag decreasing over time and alumina (Al_2O_3) content increasing due to the high affinity of the Al in the melt with oxygen (O) as shown in the following reactions.[5]

$$4Al_{steel} + 3(SiO_2)_{slag} \leftrightarrow 2(Al_2O_3)_{slag} + 3Si_{steel} \quad (1)$$

$$2Mn_{steel} + (SiO_2)_{slag} \leftrightarrow 2(MnO)_{slag} + Si_{steel} \quad (2)$$

$$2Al_{steel} + 3(MnO)_{slag} \leftrightarrow (Al_2O_3)_{slag} + 3Mn_{steel} \quad (3)$$

One objective of the industrial-scale trial evaluated in this report was to investigate different flux compositions to determine their efficacy at producing a clean casting. Internal defects in the as-cast ingot may result from deleterious flux-metal interactions. The centerline of a cast ingot is expected to have more defects than the surface, because dendritic growth occurs from the mold walls toward the center of the casting. As the dendrites grow, they produce an interconnected solid network which limits the flow of hot liquid metal through the casting giving rise to shrinkage, macrosegregation, and entrapped porosity, as shown schematically in Fig. 1. Second-phase particles that are formed during solidification such as oxides, sulfides, or nitrides can also be pushed from the dendrite growth to the centerline as well causing localized regions of poor material quality. Macrosegregation is a manifested result of this phenomenon and is considered deleterious to both processing and properties.

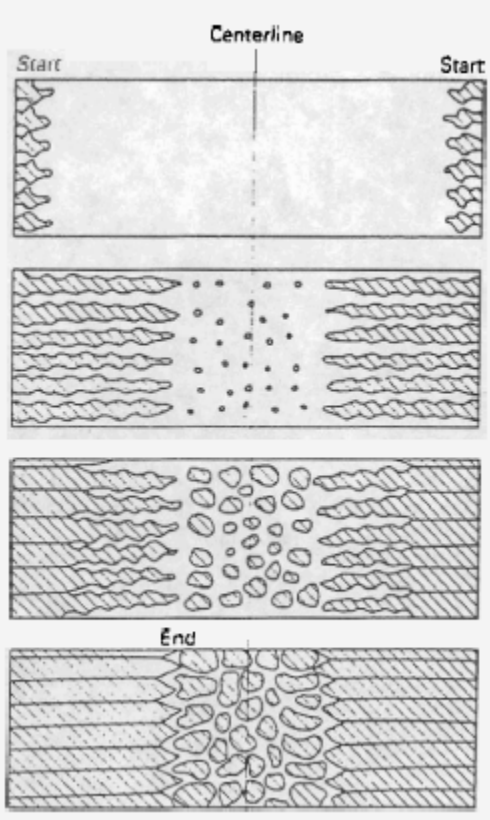

Fig. 1 Schematic of solidification of a medium freezing range alloy, indicating the development of equiaxed grains leading to dispersed porosity in the center of the casting[6]

In this report, ingots from a trial industrial heat of Fe-Mn-Al-C steel are evaluated with microscopy and compositional analysis to investigate the effect of different flux compositions on the as-cast microstructure, casting quality, and compositional stability of the ingots produced.

2. Industrial-Scale Casting and Processing

The materials evaluated in this report were from the second industrial trial heat produced by Ellwood Quality Steels (EQS), a Fe-Mn-Al-C alloy with silicon (Si) and molybdenum (Mo) additions with a target nominal composition of Fe-29Mn-9Al-1C-1Si-0.5Mo (wt%). This nominal composition is referred to as FeMnAl throughout this report. Chemistry samples were taken near the top of the ladle prior to tapping as well as both early and late in the teeming process from the melt stream. The ladle sample was evaluated at EQS using X-ray fluorescence (XRF). The early and late pour chemistry samples were analyzed at General Dynamics Land Systems (GDLS) using inductively coupled plasma optical emission spectroscopy (ICP-OES) and combustion infrared detection for C and sulfur (S). The full measured composition provided in Table 1 includes vanadium (V), chromium (Cr), nickel

(Ni), phosphorus (P), nitrogen (N), S, and boron (B) in addition to the targeted elements. The Al content appeared to decrease from the ladle to the melt stream samples; this decrease may also be attributed to the known limited accuracy of XRF at determining the Al content in a steel that also has a high Mn content. A significant change in Si content was also found, suggesting segregation of Si in the ladle. The composition analysis of Fe-Mn-Al-C alloys with high Mn and Al contents is not trivial and can vary significantly depending on the analysis technique and calibration standards used.

Table 1 Composition determined early and late in the teeming of the FeMnAl ingots

Sample	Mn	Al	Si	C	Mo	V	Cr	Ni	P	N	S	B
Ladle	29.19	9.92	0.96	0.92	0.50	0.02	0.13	0.07	0.001	0.005	0.002	0.002
Early pour	28.83	9.12	0.22	1.01	0.52	ND	0.11	0.11	ND	NT	0.0	ND
Late pour	28.72	9.09	0.60	1.01	0.53	ND	0.10	0.11	ND	NT	0.0	ND

Notes: ND = not detected; NT = not tested.

Various teeming fluxes were used in this heat to determine the ideal flux for this alloy composition and minimize deleterious flux-metal interactions. Three different fluxes were included in the present evaluation: a commercial silica-based flux, a commercial lime-alumina low-silica flux, and a custom soda-lime-alumina low-silica flux. The silica-based flux had been used in the first industrial heat of FeMnAl produced by EQS.[4] Further flux and casting details can be found in a separate report.[7]

The source ingots for this investigation were surface ground and charged for hot rolling with hot tops left intact to a temperature of 1050 ± 20 °C for hot rolling at the ArcelorMittal Coatesville facility (now owned by Cleveland Cliffs). During hot rolling two ingots experienced significant transverse (perpendicular to the rolling direction) through-thickness cracking on the first series of passes. The rolling was aborted, and the ingots were left to air cool. As shown in Fig. 2, the most severe cracking was at the slab edges on the top half of the ingot. Ingot 2 obtained 11% reduction, ingot 3 obtained 3% reduction, and the final ingot included in this study, ingot 4, had no deformation. Because ingot 4 was heated to an elevated temperature, which acted as a normalization for the composition and microstructure, it is no longer considered as in the as-cast condition. Because the amount of reduction was minimal, the centerline microstructure may not yet have been affected, and in general the depth of deformation near the surface is expected to be increasing in severity from 4 < 3 < 2.

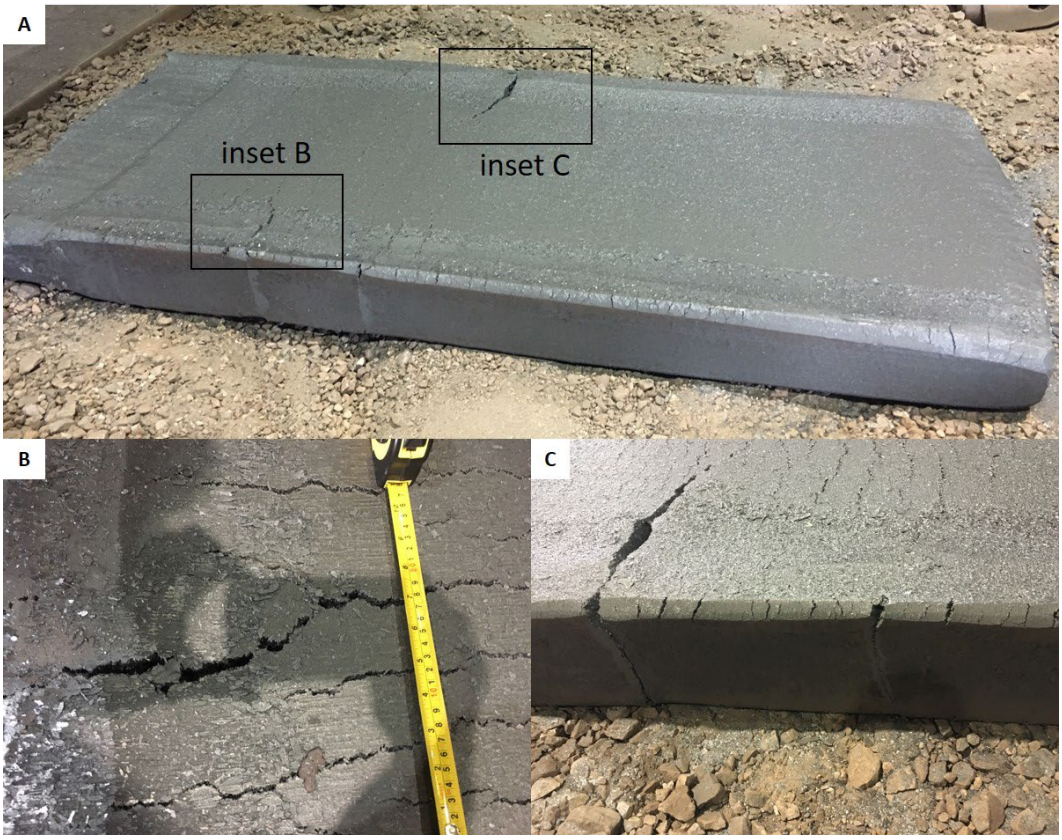

Fig. 2 Images of slab 2, after being partially broken down from an ingot. (A) The full slab with hot top visible at the left end and regions of severe cracking highlighted in (B) surface cracks with a ruler for scale and (C) severe through thickness cracking at the edge of the slab.

The combination of 1) severe cracking during rolling leading to scrapped slabs, 2) possibility of severe composition variation in the cast ingots due to segregation in the ladle, and 3) flux composition trial, made this a good opportunity to extract and evaluate both microstructure and composition variation of an industrial heat of FeMnAl in the as-cast and partially rolled conditions.

3. Sample Preparation and Experimental Approach

Sections of slabs 2 and 3 and as-normalized ingot 4 were powder cut in 3- to 5-inch-thick cross sections from the top (TOP), middle (MID), and bottom (BOT) as shown schematically in Fig. 3 and shipped to the US Army Combat Capabilities Development Command Army Research Laboratory for further sectioning and analysis.

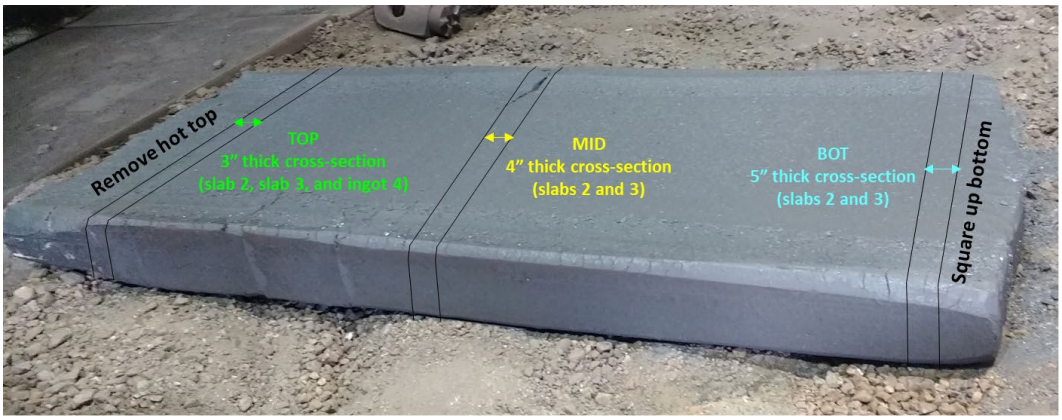

Fig. 3 As-rolled slab 2 with schematic overlay of slab sections sent to the DEVCOM Army Research Laboratory for analysis

Samples were water-jetted from each of the seven slab sections for microstructure and chemistry analysis as shown schematically in Fig. 4. Four sampling locations were evaluated: samples A and C were from the surface regions of the long 52-inch edge and short approximately 10-inch edges, respectively, sample B was from the center of the slice, and sample D was from the 10-inch dimension quarter-line, centered on the 52-inch edge. Each of these lettered samples was 1 × 1 × x-inch section thickness. A cross section for macroetching was also prepared from the top slice of ingot 4. The ingot 4 section was also used to source material for the study of the hot deformation behavior of cast FeMnAl,[8] as well as a series of blocks from the surface and centerline of the cross section that were evaluated with X-ray computed tomography for quantification of the internal defect structure.[9–11]

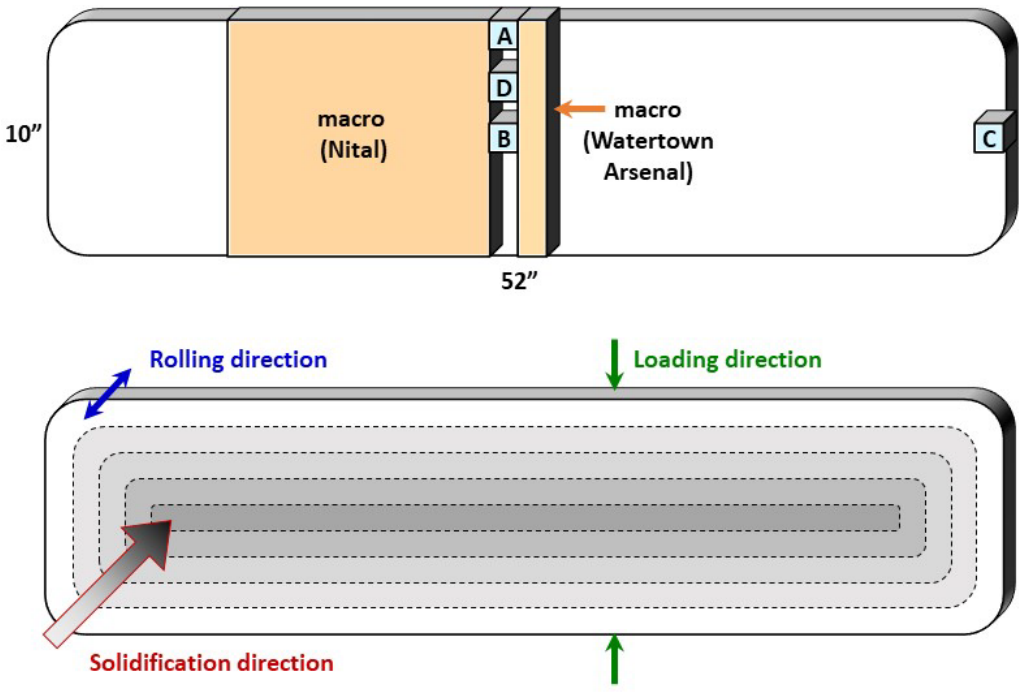

Fig. 4 Ingot/slab section schematic of the sample locations A, B, C, and D for microstructure and chemistry and macro cross section (top). Ingot/slab section schematic of the relative casting solidification direction and rolling configurations (bottom).

The samples from locations A, B, C, and D were further sectioned for microscopy and chemistry analysis as shown in Fig. 5. Using the rolling direction notation, the short-transverse face was used for microscopy analysis, denoted with an “X” in Fig. 5. The companion piece to the microscopy sample, denoted with a “Y” in Fig. 5, was sent to GDLS for composition analysis.

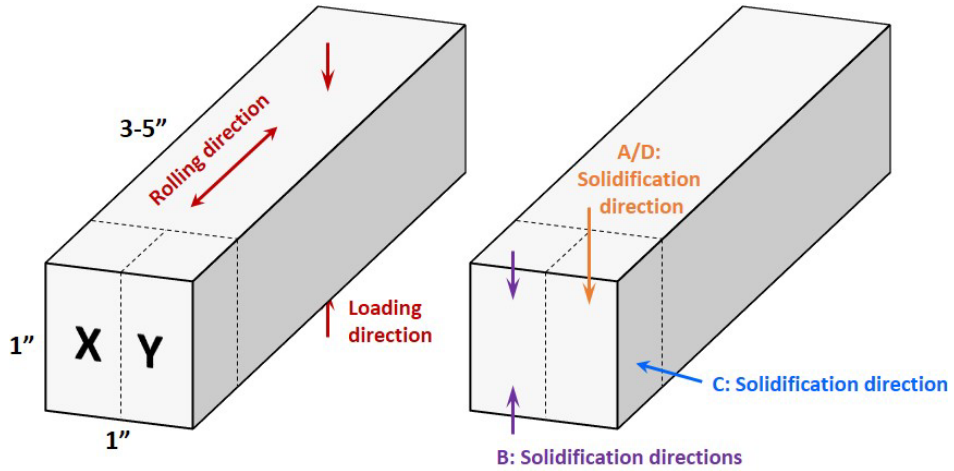

Fig. 5 Schematics for A, B, C, and D sampling of microstructure and chemistry analysis with relevant solidification and rolling directions noted. “X” indicates the face that was polished for microscopy and “Y” indicates the piece that was sent to GDLS for composition analysis.

The sampling notation used throughout this report is $IngotSection^{Sample}$. For example, $3Bot^{A}$ refers to the long-edge surface sample (A) from the bottom slice (Bot) of the third slab/ingot (3).

4. Microscopy Results

4.1 Cross-Section Macroscopy

A 10.5- × 12- × 3-inch cross section was ground and polished to an 800-grit finish with silicon carbide paper from the top slice of ingot 4 for macroetching (Fig. 4). A 5% Nital etch was used to delineate grain boundaries. A stitched image of the full 10.5-inch cross section is shown in Fig. 6. A change in microstructures is apparent around 2.3 to 3.5 inches from each edge as the etchant efficacy changed significantly here. The outer approximately 2.5 inches of the ingot consists of a dendritic microstructure as shown in the light optical microscopy (LOM) image in Fig. 7A. The transition region from 2.3 to 3.5 inches is brightly etched making it difficult to resolve microstructural features. Also beginning to appear in this transition region and continuing into the center of the ingot are dark features surrounded by high-contrast brightly etched features as shown in Fig. 7B. The center third of the ingot contains dark equiaxed grains with bright δ-ferrite appearing on many of the grain boundaries and at triple points as shown in Fig. 7C.

Fig. 6 Stitched image of a macroetched 10.5-inch cross section from the top slice of ingot 4 using 5% Nital with a centimeter ruler for scale

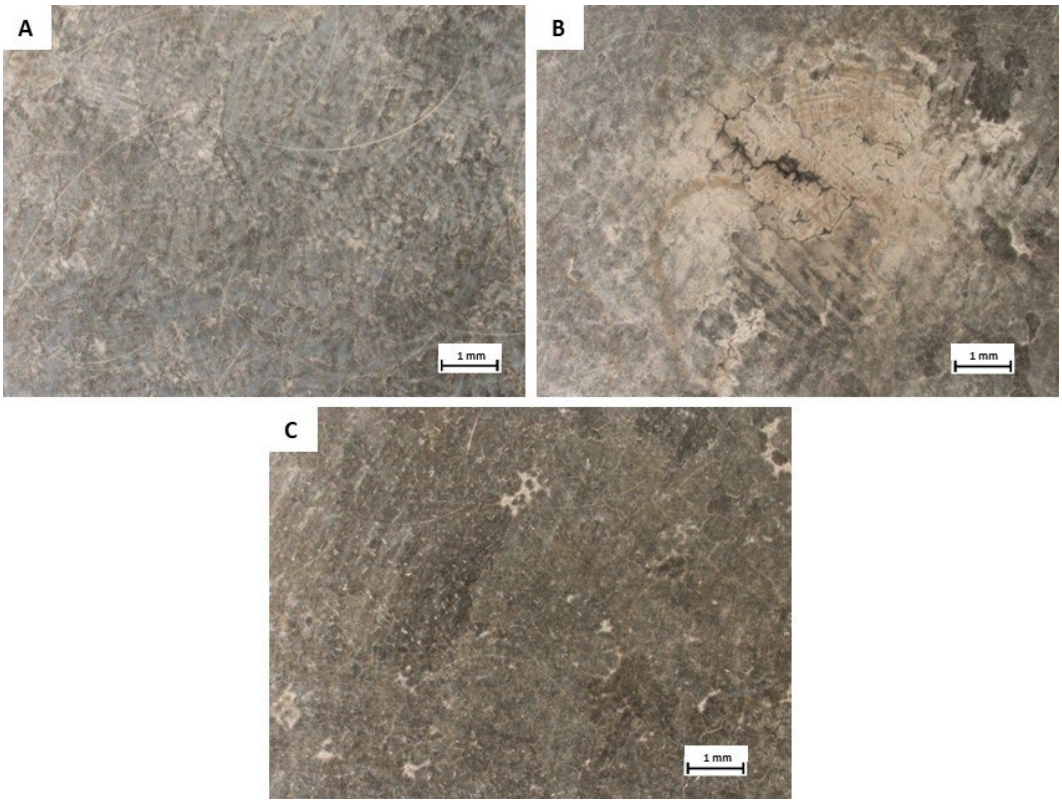

Fig. 7 Optical images taken with a 1× objective of 5% Nital macroetched cross section of the top slice of ingot 4 indicating representative microstructures. (A) Dendritic structure observed 2 inches from the surface. (B) Mixed structures and high contrast features at 3.5 inches from the surface. (C) Dark equiaxed grains with bright δ-ferrite at grain boundaries at 5.5 inches from the surface representative of the center of the ingot.

A 10- × 1- × 3-inch cross section was also waterjet cut from the ingot 4 and the 10- × 3-inch surface was polished for macroetching. An elevated temperature (50 °C) Watertown Arsenal etchant was used to identify the as-solidified grain structure and an optical image is shown in Fig. 8A. The dendritic structure extends from the mold-wall/ingot interface 2.75 inches and transitions to an equiaxed microstructure. A hardness profile of the ingot cross section, to determine if there was a variation in hardness corresponding to either segregation or microstructure, was taken and a color-coded hardness map is shown in Fig. 8B with values reported in Brinell (HBW). An increase in hardness is noted at the transitions from the columnar to equiaxed zones on either side of the ingot as well as within the center of the equiaxed region. The average center hardness was measured to be 337 ± 12 HBW. At the center of the equiaxed zone there is a high hardness area that peaks to 392 HBW and this is understood to be due to segregation of alloying elements.

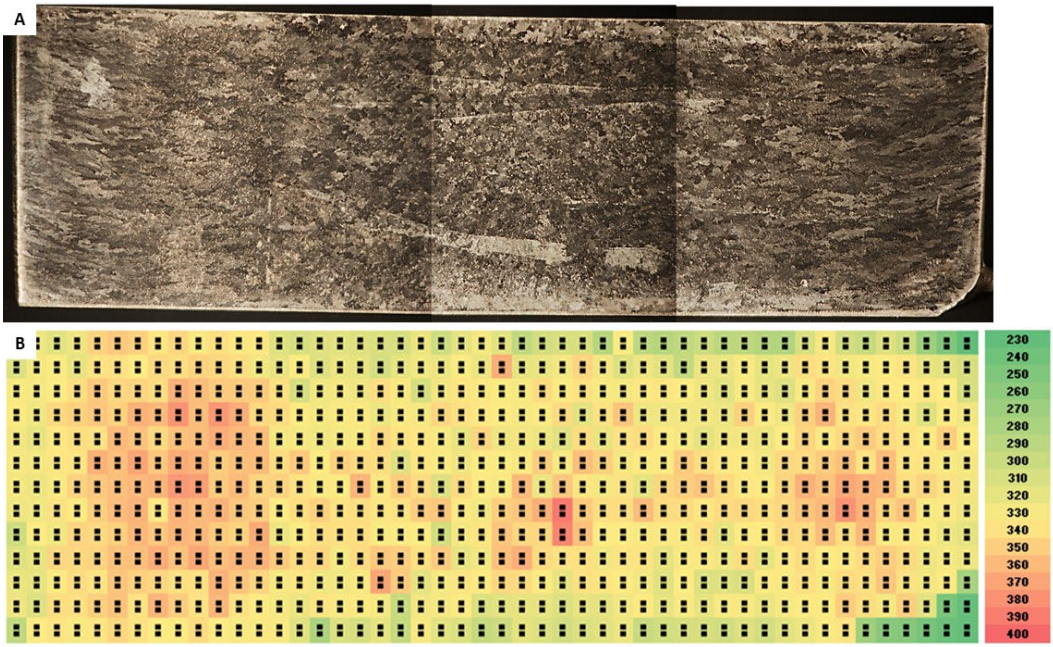

Fig. 8 (A) Macroetch of the as-cast ingot immersed in Watertown Arsenal etchant at 50 °C. (B) Hardness profile taken using Rockwell C indentions spaced 0.2 inch apart and values converted to Brinell.

4.2 Point-Specific Microscopy

Samples from the A, B, C, and D sampling locations in the top, middle, and bottom sections were polished and etched for LOM. The samples were finish polished with 0.05-µm colloidal silica and etched with 5% Nital. In general, samples A and C were similar in appearance and the section location (top/middle/bottom) appeared to have a minimal effect on the observed microstructure. Scanning electron microscopy (SEM) using backscatter detectors (BSD) as well as energy dispersive spectroscopy (EDS) was used to identify further microstructural features in the ingots.

The source slab was observed to have the largest impact on the microstructural features of the surface samples (A/C), as expected because of the difference in rolling reduction. The A and C surface samples from 4Top contained large austenitic grains with many sub-grain boundaries and no obvious δ-ferrite. Figure 9 shows LOM images of $4Top^{A}$ taken with 5× and 50× objective lenses. Samples from $4Top^{C}$ were similar in appearance to $4Top^{A}$, and a stitched SEM-BSD image in Fig. 10 shows the austenite dendrites in $4Top^{C}$ extend beyond 0.28 inch as would be expected in heavy section castings.

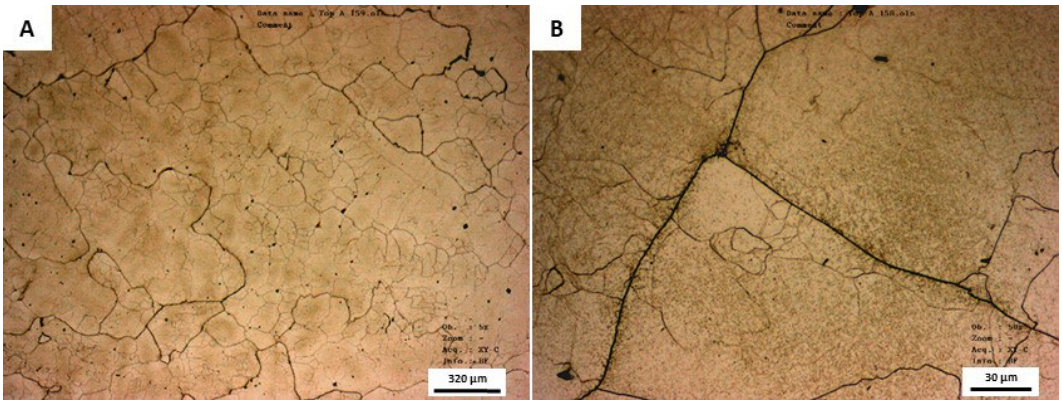

Fig. 9 Optical microscopy images of 4Top^{A}. (A) 5× objective image indicating the austenite grain size and the profusion of sub-grain boundaries. (B) 50× objective image showing more detail of the grain and sub-grain boundaries.

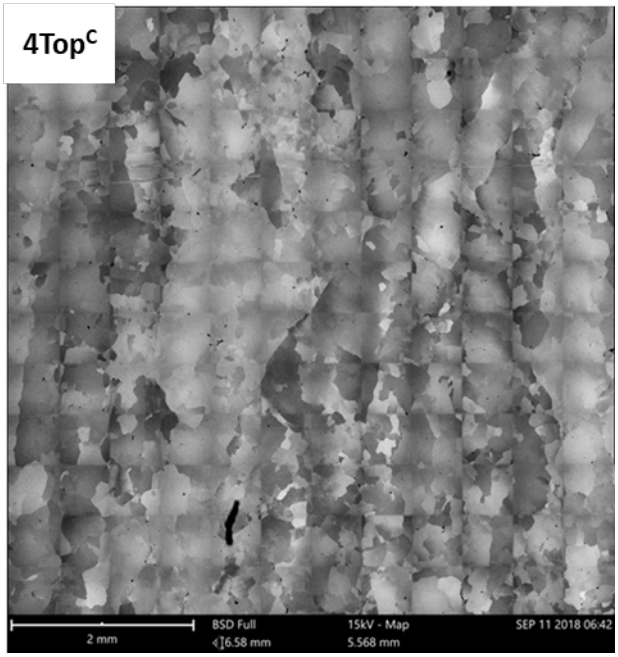

Fig. 10 Stitched SEM-BSD image of the as-cast austenite dendrites in 4Top^{C} sample with the solidification direction going up and down that extend beyond 0.28 inch in length

The A and C samples from slabs 2 and 3 had a consistent microstructure of large austenitic grains with smaller recrystallized grains on the grain boundaries as shown in the LOM images in Fig. 11. Sample 3Top^{A} had a smaller volume fraction of recrystallized grains than 3Mid^{C} as illustrated in Fig. 11A and B, respectively. Higher magnification images of the recrystallized grains are shown in Fig. 11C and D indicating the presence of twins within some of the recrystallized grains as well as a secondary phase along grain boundaries. As expected, the recrystallized grains are similar in size to the sub-grains observed near grain boundaries in the non-rolled 4Top^{A} sample.

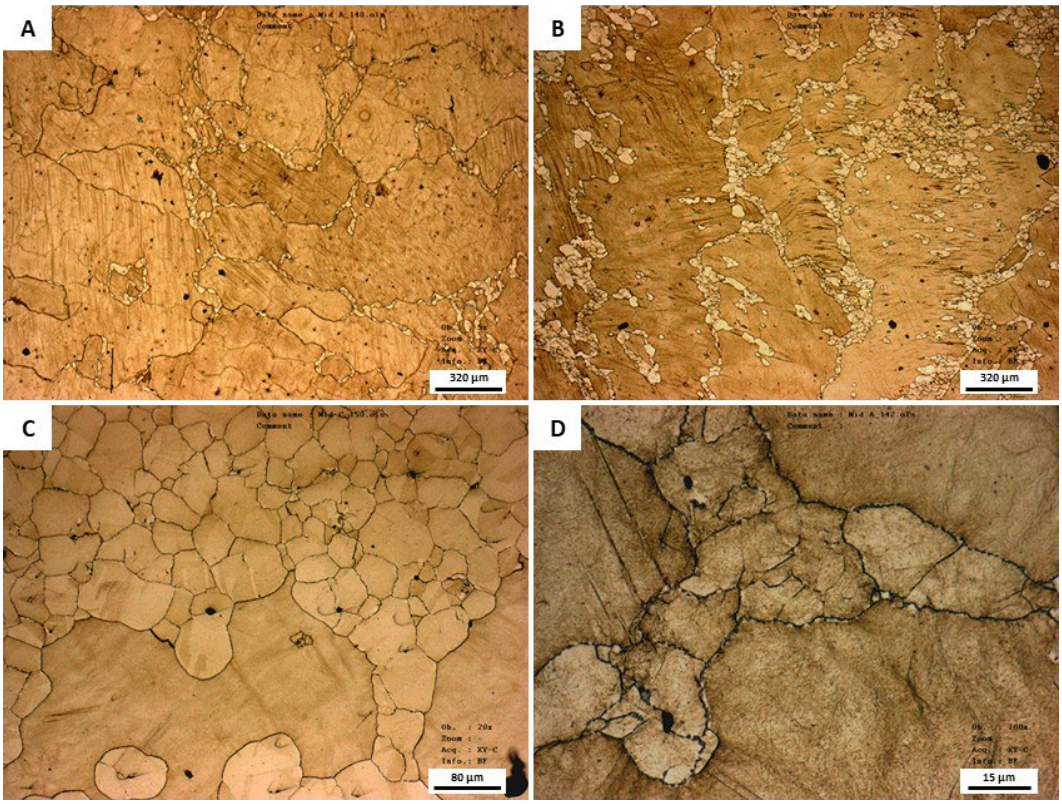

Fig. 11 Representative LOM images of microstructures found in samples A and C in Slabs 2 and 3. (A) 3Mid^{A} using a 5× objective indicating recrystallized grains at grain boundaries. (B) 3Top^{C} using a 5× objective shows a more substantial recrystallization. (C) 3Mid^{C} using a 20× objective showing equiaxed recrystallized grains. (D) 3Mid^{A} using a 100× objective indicating grain boundary and twin boundary precipitation.

Higher resolution images taken with SEM-BSD of 3Mid^{A} and 3Mid^{C} are shown in Fig. 12. The degree of strain in the BSD images is shown as a loss of image quality. This effect is associated with the strain stored in the crystal leading to a distorted scattering of electrons and is a proxy for determining the deformation within grain structure. Grains that are recrystallized show a higher-quality resolution and are differentiated from the un-recrystallized grains by both their shape that is equiaxed (shown in red arrows) and their image quality. Stitched electron images of the two samples are shown in Fig. 12C and D. A greater volume of recrystallized grains is present in the C sample compared to the A sample position. The difference in recrystallization is currently attributed to the stress state associated with the C surface. Located on the surface of the short edge, the C surface is under a more complicated stress state that led to a greater degree of deformation and allowed for more recrystallization events to occur.

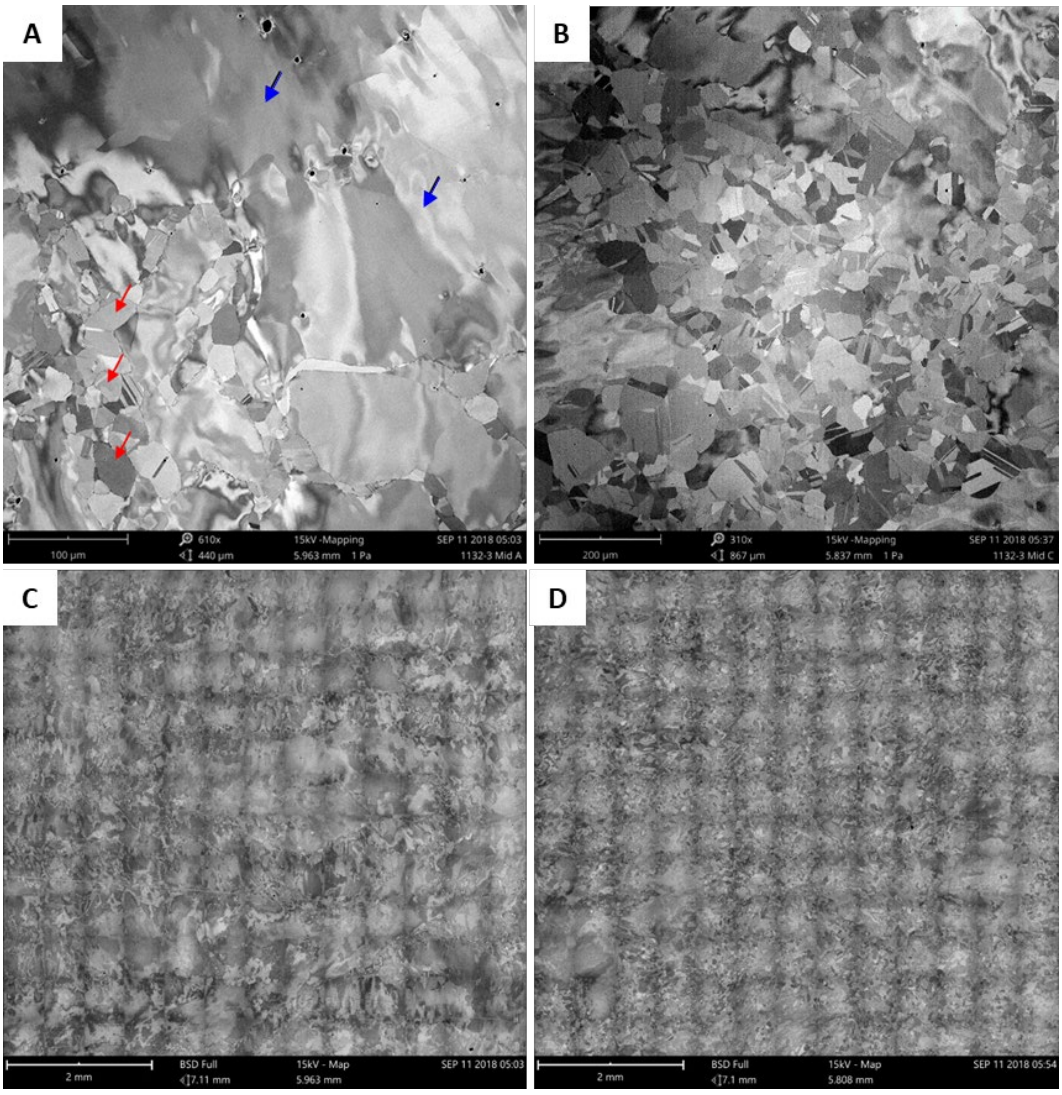

Fig. 12 BSD images of samples $3Mid^{A}$ and $3Mid^{C}$ indicating the representative microstructures found in the A and C sampling locations for slabs 2 and 3. (A) $3Mid^{A}$ with recrystallized grains highlighted by red arrows and un-recrystallized grains shown with blue arrows. (B) $3Mid^{C}$. (C) Stitched electron image of $3Mid^{A}$. (D) Stitched electron image of $3Mid^{C}$.

All of the B centerline samples had similar microstructures with large austenite grains with δ-ferrite throughout. The samples generally fell into one of two categories: 1) δ-ferrite appears in a dendritic structure ($2Top^{B}$ and $3Top^{B}$) as shown in Fig. 13A, and 2) smaller quantities and random distribution of δ-ferrite as shown in Fig. 13B. Both of these microstructures are representative of as-cast centerline microstructures. Because of the limited amount of deformation induced during the partial rolling of slabs 2 and 3, the centerline is unaltered during the ingot breakdown, which is confirmed from the lack of deformation observed from the δ-ferrite dendrites retained from the cast structure. At increased magnification, jagged

grain boundaries decorated with secondary phases were observed as shown in Fig. 13C. Additionally, some of the δ-ferrite grains showed the initial signs of the transformation to austenite starting near the grain boundaries and propagating into the grain as shown in Fig. 13D.

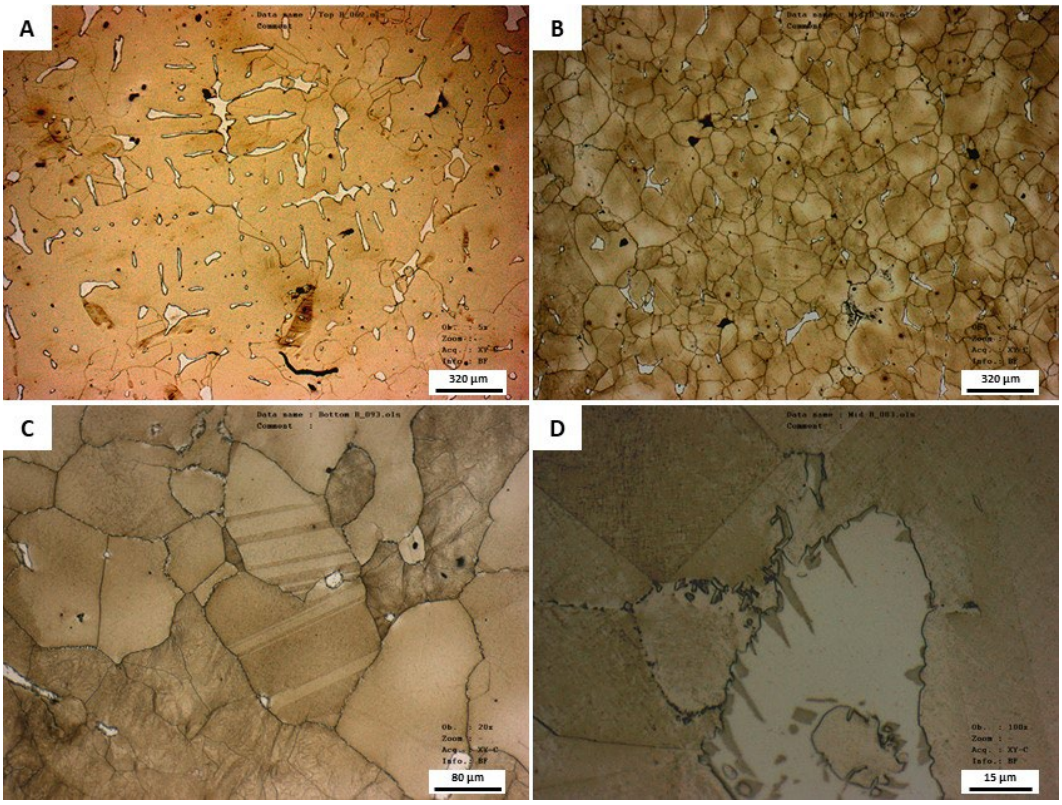

Fig. 13 Representative LOM images of FeMnAl B samples. (A) 5× objective with δ-ferrite appearing in a dendritic pattern as seen only in the "Top" slices of slabs 2 and 3. (B) 5× objective 2Mid^{B} representative of the broken δ-ferrite distribution seen in the remaining sections. (C) 20× objective 2Bot^{B} showing both δ-ferrite and jagged grain boundaries decorated with a secondary phase. (D) 100× objective 2Mid^{B} showing more detail of the secondary phases on grain boundaries and austenite growth into δ-ferrite.

The quarter-line sample, sample D was only obtained and analyzed from 4Top^{D}. As shown in Fig. 14, there are occasional small islands of δ-ferrite as well as secondary phases and pores along grain boundaries. In the 100× LOM image a basket weave pattern is observed within the austenite grains, which may be evidence of coarse κ-carbide forming during cooling.

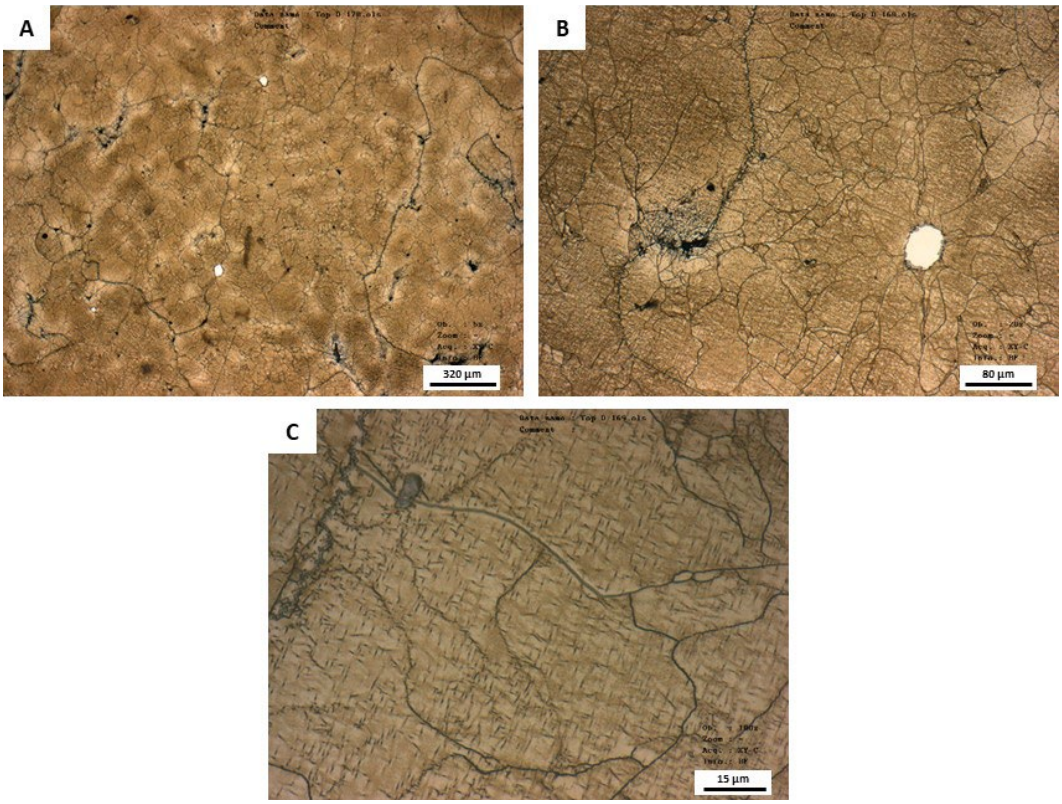

Fig. 14 LOM images of 4Top^{D} taken with (A) 5× objective lens, (B) 20× objective lens, and (C) 100× objective lens

Second-phase particles were observed to occur at the austenite grain boundaries throughout the ingot and an example micrograph is shown in Fig. 15. These second-phase particles are a consequence of the eutectoid decomposition of austenite transforming to α-ferrite and κ-carbide. SEM images of the intergranular carbide are shown in Fig. 15 with the location of the EDS analysis shown with red plus (+) signs. The second-phase particle was measured to contain 17 at% C, 14 at% Al with the remainder being Fe and Mn, which is expected for κ-carbide with composition of $(Fe,Mn)_3AlC$; however, measuring C using EDS is inaccurate. Because the alloy was treated with magnesium (Mg) to modify oxides and remove sulfur, magnesium-based inclusions were also found in the steel and a complex Mg-type inclusion that co-precipitated with a Mo/zirconium (Zr) type carbide is show in Fig. 15C with the measured composition shown in Table 2.

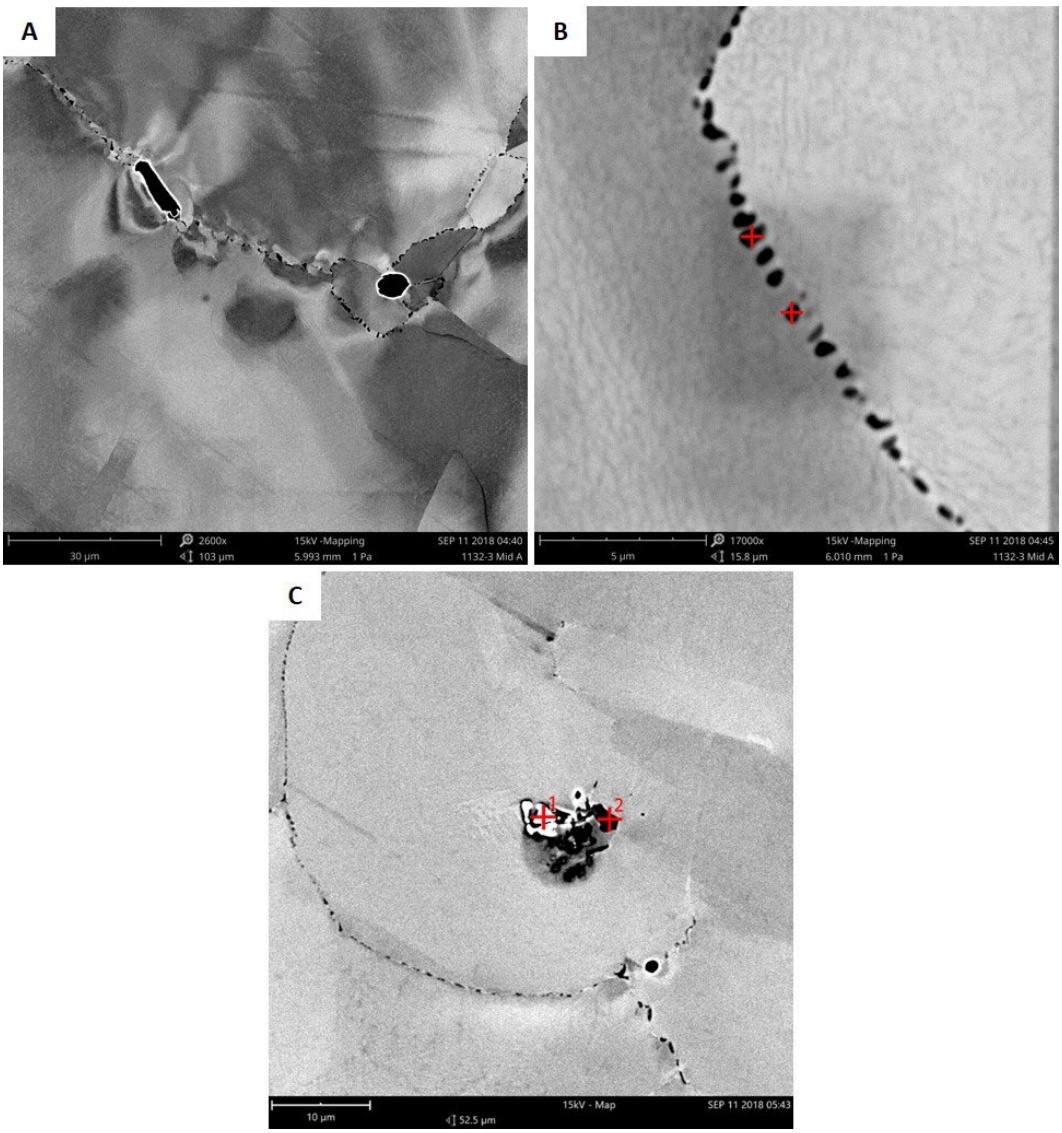

Fig. 15 SEM image of grain boundary second-phase particles in 3Mid^{A} at (A) low magnification, (B) high magnification with EDS spectrum location denoted by red plus (+) with a nominal composition of representative of κ-carbide, and (C) SEM image of a complex inclusion and carbide formed in 3Mid^{C} with EDS spectrum locations denoted by a numbered plus (+) with compositions in Table 2.

Table 2 Composition of the particles found within sample 3Mid^{C} as identified in Fig. 15C using EDS analysis with composition values given in weight percent

Particle	Mo	Zr	Mg	Mn	Ti	Nb	O	C
1	33.6	14.7	0.94	7.0	9.1	2.9	6.5	13.2
2	. . .	. . .	24.7	18.6	. . .	. . .	17.6	0.5

Note: Ti = titanium, Nb = niobium.

5. Calculation of Phase Diagram (CALPHAD) Modeling

Scheil solidification models and equilibrium phases were calculated with ThermoCalc 2020a using the TCFE9 database for the compositions from Table 1, excluding impurities of less than 0.01 wt% (N, S, P, and B). The melt composition during teeming was consistent for all elements except Si, which increased from 0.22 to 0.60 mass percent from early to late during ingot teeming. Scheil simulations were performed with C as a fast-diffusing element and terminated at 0.95 mol fraction solid, as any further solidification results are typically considered irrelevant to observed composition gradients in high alloy steel solidification.

The Scheil simulation results, shown in Fig. 16, indicate that only two solid phases are formed during solidification. The first phase to solidify is δ-ferrite (body-centered cubic [BCC]), starting around 1345 °C and then the peritectic formation of austenite (face-centered cubic [FCC]) starting around 1280 °C. The composition variation affected the liquidus and solidus temperatures by changing them by less than 20 °C as shown in Table 3. The Scheil simulation does not account for the peritectic reaction of δ-ferrite + liquid forming austenite during the solidification process, predicting a casting with a significantly higher δ-ferrite content than is observed.

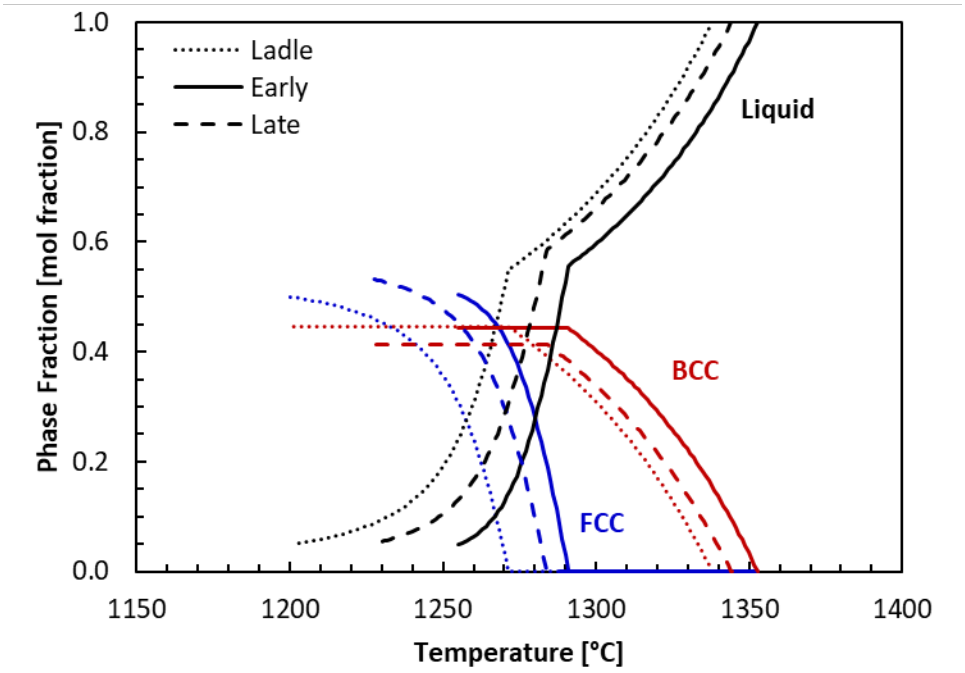

Fig. 16 Scheil simulation results for Fe-Mn-Al-C steel using the three measured compositions performed in ThermoCalc with the TCFE9 database indicating only two solid phases form during solidification to 95 mol % solid: δ-ferrite (BCC) and austenite (FCC)

Table 3 Critical solidification temperatures (°C) for the liquidus, peritectic, and solidus (at 95 mol % solid) determined by Scheil simulations for experimentally measured compositions

Temperature	Ladle	Early	Late
Liquidus	1337.93	1352.85	1344.28
Peritectic	1271.29	1291.08	1283.77
Solidus (95%)	1199.26	1255.05	1226.74

Equilibrium calculations were also performed in ThermoCalc for 1 mole of material at 1 atm pressure over the temperature range from 500 to 1200 °C. The CUB_A13 phase was rejected from the simulations, as this β-Mn phase is not observed in practice. The equilibrium simulation results are consistent at high temperatures for both the early and late compositions, with both compositions having a fully austenitic phase field starting at 1002 °C as seen in Fig. 17. Compositionally induced variation is seen in the phase nucleation start temperatures for κ-carbide, α-ferrite, and M_6C. The "late" composition had significantly more Si, which is a ferrite stabilizer and also a primary constituent in the M_6C carbide. The late composition was also predicted to have a higher nucleation start temperature for κ-carbide, in agreement with past studies showing that Si increases the kinetics of κ-carbide formation in Fe-Mn-Al-C alloys.[12] Equilibrium simulation results of the phase nucleation and transformation temperatures have been reported in Table 4 for clarity.

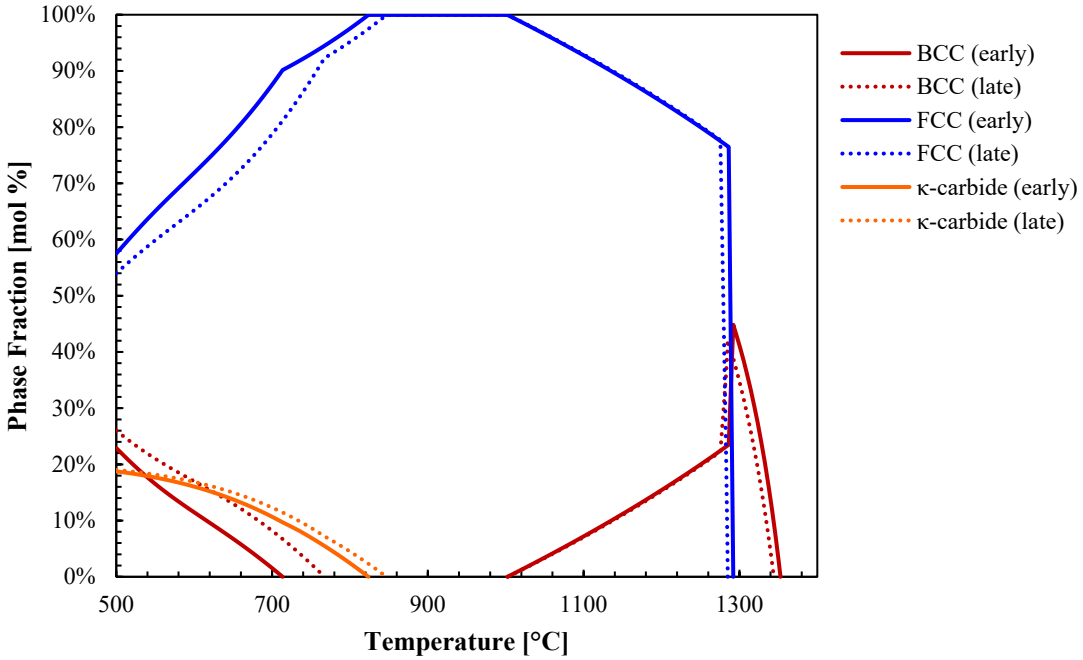

Fig. 17 Equilibrium ThermoCalc simulation results of major solid phases (ferrite [BCC], austenite [FCC], and κ-carbide) present for early and late teeming chemistries

Table 4 ThermoCalc predicted equilibrium phase formation start temperatures and transformation finish temperatures in the 500–1400 °C temperature range for the early and late teeming compositions

Phase	Nucleation start temperature (°C)		Transformation finish temperature (°C)	
	Early	Late	Early	Late
δ-ferrite (BCC)	1353	1344	1002	1002
Austenite (FCC)	1292	1285	. . .	. . .
κ-carbide	824	847	. . .	. . .
M_6C	735	849	. . .	. . .
α-ferrite (BCC)	714	767	. . .	. . .

Table 5 reports the equilibrium simulation results for the phase fractions at 500 and 1050 °C. At the nominal rolling temperature of 1050 °C both the early and late compositions were predicted to have around 4.5 vol% δ-ferrite present with the remainder as austenite. While the presence of secondary phases can be a cause for cracking during rolling, these equilibrium values were not likely achieved and had a less significant impact than the hot workability of the austenite matrix at this temperature. At a 500 °C aging temperature, both the early and late compositions are predicted to have similar equilibrium volume fractions of κ-carbide and M_6C, although the late composition was generally predicted to have higher precipitate volume fractions in addition to a higher volume fraction of stable α-ferrite.

Table 5 ThermoCalc predicted equilibrium phase volume fractions at 500 and 1050 °C for early and late teeming compositions

Phase	% V_f at 500 °C		% V_f at 1050 °C	
	Early	Late	Early	Late
α-ferrite (BCC)	23.17	26.39	. . .	. . .
δ-ferrite (BCC)	. . .	. . .	4.54	4.44
Austenite (FCC)	59.52	55.90	95.46	95.56
κ-carbide	16.55	16.83	. . .	. . .
M6C	0.76	0.88	. . .	. . .

6. Chemistry Results

Chemistry samples as identified in Fig. 5 were analyzed at GDLS using ICP-OES and combustion C/S analysis. The complete set of measured values are reported in Table 6. The heat chemistry, determined as an average of all the measured values, is Fe-31.46Mn-8.52Al-0.32Si-0.98C-0.51Mo-0.11Ni-0.09Cr (wt%). Not shown are S and V that were also measured but were consistently below the detection limit (0.001 wt%). Ni, Cr, and P content were generally consistent across all sampling locations. Variation was observed for Mn, Al, Si, C, and Mo. Because of its atomic

size, Mo has been noted historically to have a high segregation ratio in industrial-scale castings of high-strength steels for Mo contents comparable to those in this alloy.[13]

Table 6 Measured chemistry values of Fe-Mn-Al-C (in wt%)

Ingot	Slice	Location	Notation	Mn	Al	Si	C	Mo	Ni	Cr	P
2	Top	A	$2Top^{A}$	31.37	8.94	0.31	1.00	0.53	0.11	0.09	<0.001
	Middle		$2Mid^{A}$	30.14	8.96	0.17	1.00	0.53	0.11	0.09	<0.001
	Bottom		$2Bot^{A}$	32.97	9.07	0.26	0.99	0.54	0.11	0.09	0.001
2	Top	B	$2Top^{B}$	29.81	8.88	0.16	0.82	0.50	0.11	0.09	<0.001
	Middle		$2Mid^{B}$	30.65	8.84	0.17	1.01	0.53	0.11	0.09	<0.001
	Bottom		$2Bot^{B}$	32.65	8.82	0.29	1.00	0.53	0.11	0.09	0.001
2	Top	C	$2Top^{C}$	32.35	8.71	0.23	0.99	0.53	0.11	0.09	<0.001
	Middle		$2Mid^{C}$	32.00	8.61	0.51	0.99	0.53	0.11	0.09	0.001
	Bottom		$2Bot^{C}$	32.06	8.70	0.23	0.99	0.52	0.11	0.09	<0.001
3	Top	A	$3Top^{A}$	31.58	8.46	0.44	0.99	0.52	0.11	0.09	0.001
	Middle		$3Mid^{A}$	31.44	8.47	0.31	1.01	0.51	0.11	0.09	0.002
	Bottom		$3Bot^{A}$	31.27	8.46	0.34	0.99	0.51	0.11	0.09	0.003
3	Top	B	$3Top^{B}$	30.51	8.64	0.46	0.78	0.47	0.11	0.08	0.003
	Middle		$3Mid^{B}$	31.40	8.39	0.42	1.00	0.51	0.11	0.09	0.001
	Bottom		$3Bot^{B}$	31.72	8.41	0.45	0.99	0.50	0.11	0.08	0.002
3	Top	C	$3Top^{C}$	31.24	8.19	0.20	0.98	0.50	0.11	0.08	0.002
	Middle		$3Mid^{C}$	31.55	8.25	0.25	0.99	0.50	0.11	0.08	0.003
	Bottom		$3Bot^{C}$	31.21	8.09	0.24	0.99	0.49	0.11	0.08	<0.001
4	Top	A	$4Top^{A}$	30.86	8.03	0.42	0.99	0.50	0.11	0.08	0.002
		B	$4Top^{B}$	30.48	8.33	0.40	1.00	0.48	0.11	0.08	0.002
		C	$4Top^{C}$	32.39	8.06	0.54	1.02	0.48	0.12	0.08	0.002
		D	$4Top^{D}$	32.48	8.10	0.31	1.00	0.50	0.11	0.08	<0.001

Statistical correlation analysis (n = 22) was performed on the measured chemistry values to determine the statistically significant correlations as shown in Fig. 18. Significant correlations are considered to have a p-value ≤0.05. Five significant correlations are observed: ingot-Al, ingot-Si, ingot-Mo, Mn-C, and Mo-Al.

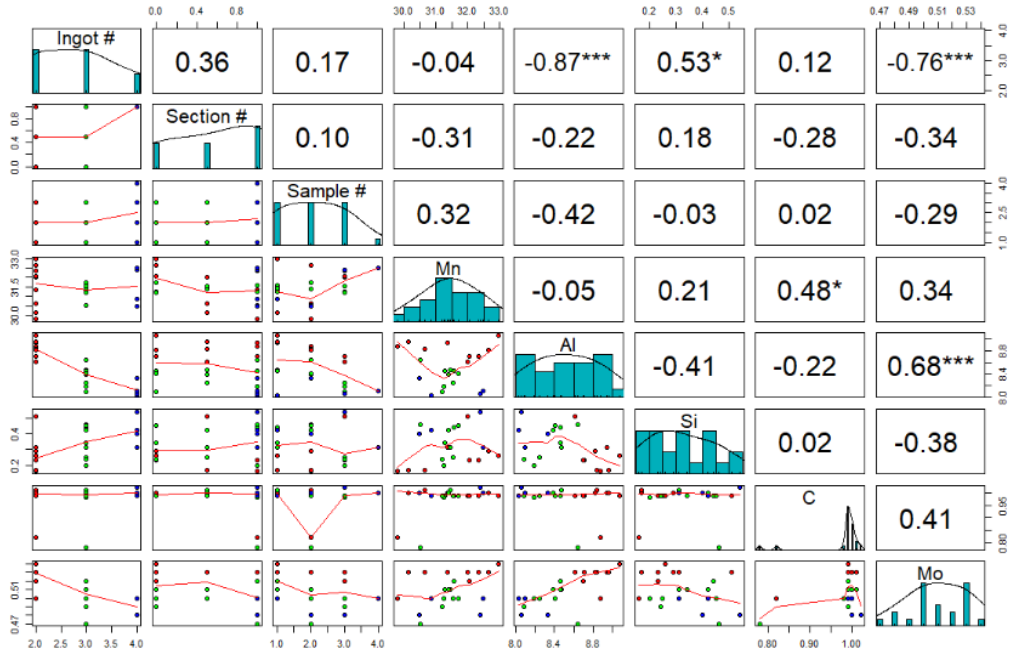

Fig. 18 Pairwise scatterplot of all considered variables including: ingot number, section ID (0 = BOT, 0.5 = MID, 1 = TOP), sampling ID (1 = A, 2 = B, 3 = C, 4 = D), and primary composition elements. The distribution of each variable is shown in a histogram on the diagonal. The lower triangle consists of scatter plots with locally smoothed regressions, where symbol color also indicates the ingot number (red = 2, green = 3, blue = 4). The upper triangle consists of the Pearson correlation coefficient and significance level. Asterisk notation is used for p-value significance ($p \leq 0.001$ = ***, $p \leq 0.01$ = **, $p \leq 0.05$ = *, and no symbol for $p > 0.05$).

Although Mn had some minor fluctuation in values, 31.46 ± 0.35 wt% (deviation based on a 95% confidence interval [95% CI]), the fluctuations were not correlated to the ingot, section, or sampling location and are representative of general alloy segregation. Similarly, C had minor fluctuations in value (0.98 ± 0.02 wt%) with no correlation to ingot, section, or sampling location and had two low outlying values from samples taken in the center sampling location "B". Although neither Mn nor C showed a statistical significance in composition as a function of sampling site, the results were positively correlated with each other. This is indicative of the strong binding between Mn and C within the steel resulting in co-segregation, as has been predicted with density functional theory calculations.[14]

The overall Al content was 8.52 ± 0.13 wt% and was strongly negatively correlated to ingot number. Al values decreased from ingot 2 > 3 > 4, with no significant change from top to bottom of the ingot or sampling location. Si content (0.32 ± 0.05 wt%) was also strongly correlated to ingot number but had a positive correlation. This is the reverse correlation as was observed for Al. The changes in Al and Si content as a function of ingot number is indicative of either flux-alloy

interaction or changes in melt chemistry during teeming as a function of ladle segregation. Ladle segregation would also require variation in the composition from the top to the bottom of the ingot. These relationships are explored in Fig. 19 where for a given ingot, the Al and Si concentrations are shown not to shift on average. Further, the TOP section where the largest influence of flux would be observed has no significant deviation from the MID and BOT sections. The Al and Si relationships with the flux compositions and precise teeming order are explored in further detail in a separate report.[7]

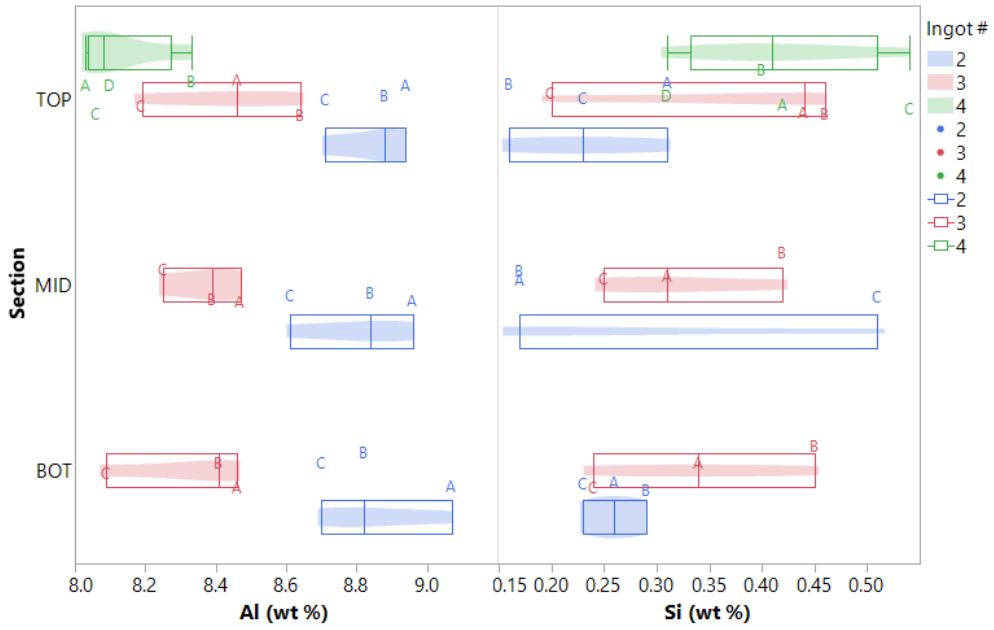

Fig. 19 Overlaid data points and violin and box plots for Al and Si content as a function of ingot section and ingot number. Points are represented by their sampling location letter designation.

Interestingly, despite Mo having a very small range in measured values, 0.51 ± 0.01 wt%, which would be considered insignificant in steelmaking, a strong negative correlation was observed with ingot number as well as a strong positive correlation with Al. There is no previous indication of co-segregation of Al and Mo. Mo has been reported to co-segregate with P and when evaluating the pairwise correlation between Mo and P a significant positive correlation was found.

7. Conclusion

The second industrial trial heat of FeMnAl ingot casting performed at EQS with subsequent hot rolling at ArcelorMittal Coatesville (now Cleveland Cliffs) provided a unique opportunity to extract and evaluate the microstructure and chemical segregation within these large castings. The flux trial performed during

the ingot casting used five unique flux compositions, three of which were included in the sampling for this analysis. The severe cracking during hot rolling that led to scraped slabs enabled the destructive evaluation of the ingot and slab microstructure with three different levels of deformation, from 0% to 11% reduction.

Composition variation in the ingots showed that Mn and C were positively correlated, although there was no spatial significance in their variation. Ingot number was strongly correlated to Al (negative) and Si (positive). Further investigation showed no significant change in Al or Si concentration through the length of a given ingot suggesting that ladle segregation was not the root cause, despite the original compositions measured from the early and late teeming samples. Because the top section, where the flux composition would have the largest effect, was also not significantly different from the middle or bottom sections, the teeming flux composition is suggested also to not have a significant effect on the ingot composition for the fluxes evaluated in this study.

The microstructure of the ingots was consistent with that of a medium freezing range alloy. The Watertown Arsenal etchant worked well for macroscopic investigations and the Nital etchant was preferred for microscopy. A larger volume fraction of δ-ferrite was found in the top sections of the ingots suggesting nonuniform cooling rates through the height of the ingot despite the presence of a hot top.

8. References

1. Howell RA, Gerth R. Fe-Mn-Al-C Alloy steels - a new armor class. SAE International; 2017. SAE Technical Paper 2017-01-1703. doi:10.4271/2017-01-1703.

2. Limmer KR, Horwath EJ, Field DM. Ballistic performance of industrial production lightweight FeMnAl armor steel. DEVCOM Army Research Laboratory; 2020 Nov. Report No.: ARL-TR-9107.

3. Horwath EJ, Limmer KR, Cheeseman BA. Lightweight FeMnAl armor steel: material development and ballistic performance. Army Research Laboratory (US); 2018 Aug. Report No.: ARL-TR-8459.

4. Limmer KR, Ligda JP, Cheeseman BA. First industrial trial production of a low-density austenitic wrought steel plate. CCDC Army Research Laboratory; 2019 Dec. Report No.: ARL-TR-8873.

5. Bausch M, Frommeyer G, Hofmann H, Balichev E, Soler M, Didier M, Samek L. Ultra high-strength and ductile FeMnAlC light-weight steels. European Commission, Directorate-General for Research and Innovation; 2013. doi:10.2777/33040.

6. Richards VL. Chapter 4: Risering of castings. Missouri University of Science and Technology. 2013;MET 307.

7. Limmer KR, Field DM, Sebeck KM, Kane J, DeGenova J, Thompson P, Schwartz D. Industrial-scale practice for casting Fe-Mn-Al-C ingots. DEVCOM Army Research Laboratory; 2022 May. Report No.: ARL-TR-9457.

8. Pierce DT, Field DM, Limmer KR, Muth T, Sebeck KM. Hot deformation behavior of an industrially cast large grained low density austenitic steel. Mater Sci Eng A. 2021;825:141785.

9. Green WH, Cheeseman BA, Field DM, Limmer KR. Comprehensive assessment of overall quality of several specimens from an as-cast FeMnAl steel alloy ingot via X-ray computed tomography. CCDC Army Research Laboratory; 2020 July. Report No.: ARL-TR-9000.

10. Green WH, Cheeseman BA, Field DM, Limmer KR. Advanced X-ray computed tomography of voids and porosity in as-cast FeMnAl steel alloy material. CCDC Army Research Laboratory; 2020 June. Report No.: ARL-TR-8975.

11. Green WH, Cheeseman BA, Field D, Limmer KR. Quantitative analysis of porosity and voids in cast Fe-Mn-Al steel alloy material via X-Ray computed tomography. 46th Annual Review of Progress in Quantitative Nondestructive Evaluation; 2019.

12. Bartlett LN, Van Aken DC, Medvedeva J, Isheim D, Medvedeva NI, Song K. An atom probe study of kappa carbide precipitation and the effect of silicon addition. Metall Mater Trans A Phys Metall Mater Sci. 2014;45(5):2421–2435. doi:10.1007/s11661-014-2187-3.

13. Poirier DR, Flemings MC. Investigation of solidification of high-strength steel castings. Massachusetts Institute of Technology; 1965. Report No.: AMRA CR 63-04/4.

14. Medvedeva NI, Park MS, Van Aken DC, Medvedeva JE. First-principles study of Mn, Al and C distribution and their effect on stacking fault energies in fcc Fe. J Alloys Compd. 2014;582:475–482.

List of Symbols, Abbreviations, and Acronyms

Al	aluminum
Al_2O_3	alumina
ARL	Army Research Laboratory
B	boron
BCC	body-centered cubic
BSD	backscatter detection
C	carbon
CALPHAD	calculation of phase diagrams
Cr	chromium
DEVCOM	US Army Combat Capabilities Development Command
EDS	energy dispersive spectroscopy
EQS	Ellwood Quality Steels
FCC	face-centered cubic
Fe	iron
FeMnAl	iron-based alloy with nominal composition of Fe-29Mn-9Al-1Si-1C-0.5Mo in wt%
GDLS	General Dynamics Land Systems
HBW	Brinell hardness
ICP-OES	inductively coupled plasma optical emission spectroscopy
LOM	light optical microscopy
Mn	manganese
Mo	molybdenum
N	nitrogen
Ni	nickel
O	oxygen
P	phosphorus
RHA	rolled homogeneous armor
SEM	scanning electron microscopy
S	sulfur

Si	silicon
SiO_2	silica
V	vanadium
XRF	X-ray fluorescence
Zr	zirconium

1 (PDF)	DEFENSE TECHNICAL INFORMATION CTR DTIC OCA
1 (PDF)	DEVCOM ARL FCDD RLD DCI TECH LIB
6 (PDF)	DEVCOM ARL FCDD RLW M B CHEESEMAN K CHO FCDD RLW MF K LIMMER D FIELD K DOHERTY M WALOCK
4 (PDF)	DEVCOM GVSC FCDD GVS IEE MA J HEADING K SEBECK I TOPPLER K VIEAU